

# In-flight Energy Calibration of the GECAM Gamma-ray Detectors

Rui Qiao¹®, Dong-Ya Guo¹, Wen-Xi Peng¹,², Yan-Qiu Zhang¹,², Shuo Xiao¹,², Shao-Lin Xiong¹, Chao Zheng¹,², Chao-Yang Li¹,³, Jia-Cong Liu¹,², Wang-Chen Xue¹,², Jian-Jian He¹, Zheng-Hua An¹, Da-Li Zhang¹, Xin-Qiao Li¹, Li-Ming Song¹®, Shi-Jie Zheng¹, Ke Gong¹, Ya-Qing Liu¹, Xin-Ying Song¹, Xiao-Yun Zhao¹, Xiang-Yang Wen¹, Yan-Bing Xu¹, Xiang Ma¹, Xiao-Bo Li¹, Ping Wang¹, Yue Huang¹®, Ce Cai¹,², Qi-Bin Yi¹,⁴, Yi Zhao¹,⁵, and Chen-Wei Wang¹,² Institute of High Energy Physics, Chinese Academy of Sciences, Beijing 100049, China; qiaorui@ihep.ac.cn, guody@ihep.ac.cn, pengwx@ihep.ac.cn University of Chinese Academy of Sciences, Beijing 100049, China Sciences, Beijing 100049, China West Normal University, Xiangtan 411105, China Beijing Normal University, Beijing 100875, China

#### **Abstract**

The Gravitational wave high-energy Electromagnetic Counterpart All-sky Monitor (GECAM) mission is designed to monitor the Gamma-Ray Bursts (GRBs) associated with gravitational waves and other high-energy transient sources. The mission consists of two microsatellites which are planned to operate at the opposite sides of the Earth. Each GECAM satellite could detect and localize GRBs in about 8 keV–5 MeV with its 25 Gamma-Ray Detectors (GRDs). In this work, we report the in-flight energy calibration of GRDs using the characteristic gamma-ray lines in the background spectra, and show their performance evolution during the commissioning phase. Besides, a preliminary cross-calibration of energy response with Fermi GBM data is also presented, validating the energy response of GRDs.

Key words: (stars:) gamma-ray burst: general – instrumentation: detectors – methods: data analysis

#### 1. Introduction

The coincident observations of gravitational wave (GW) event GW170817 and its electromagnetic (EM) counterpart GRB 170817A (Meegan et al. 2009; Abbott et al. 2017; Savchenko et al. 2017) herald a new era of multi-messenger gravitational-wave astronomy. Indeed, gamma-ray observation played a crucial role in this event in terms of the identification and localization of this GW event: Fermi/GBM was triggered even before the finding of GW170817 and provided a raw location in about a 25 s post-trigger which was followed by a finer location in three hours (Von Kienlin et al. 2017). These locations reported by Fermi/GBM helped the follow-up observations of this event in multi-wavelength.

In order to capture these rare but important GW EM counterparts, GECAM was proposed to detect and localize GRBs in about 8 keV–5 MeV. The GECAM mission consists of two identical microsatellites (GECAM-A and GECAM-B) which are planned to be operating at the same orbit (altitude 600 km, inclination angle 29°) with opposite phase around the Earth. Each satellite is equipped with 25 Gamma-Ray Detectors (GRDs) and eight Charge-Particle Detectors (CPDs). The 25 GRDs are installed almost uniformly with different orientations on the detector dome of the satellite (Li et al. 2022). Each GRD has a field-of-view (FOV) of approximately  $2\pi$  steradians, and one satellite has an FOV approximately  $2.75\pi$  steradians. So the FOV of two satellites can cover 100% all-sky without the

occultation of the Earth. With the on-board trigger and localization software of GECAM (Zhao et al. 2021), GECAM can be triggered by GRBs in real-time, and the trigger time and location of GRB will be calculated on-board and sent to ground within about 1 minute, while more data including light curves and spectra within about 10 minutes through the BeiDou navigation system. After the bulk telemetry data is arrived, the refined analysis results will be implemented automatically and manually.

In this work, we focus on the on-orbit energy calibration of GRDs. In Section 2, a brief description of GRDs is given. The in-flight performance and the background spectra used for energy calibration are presented in Section 3. In Sections 4 and 5, we describe the in-flight calibration procedures and results of energy-channel and energy resolution, respectively. In Section 6, we introduce the detector response matrix generation and the cross-calibration results compared with Fermi/GBM observation.

### 2. Gamma-Ray Detectors Onboard GECAM

Each GRD module consists of a LaBr3:Ce scintillator ( $\phi$  76 mm  $\times$  15 mm) readout by a dedicated SiPM array (An et al. 2022). The LaBr3:Ce crystal is a high light yield scintillator with good energy resolution (typically <3% FWHM at 662 keV) (Moses 2002; Iltis et al. 2006). The high stability of the light yield against temperature fluctuation (Moszynski et al. 2006;

Normand et al. 2007) and radiation tolerance (Owens et al. 2007a; Drozdowski et al. 2007; Ramilli 2009) are merits of its application in space projects, such as the CALET mission (Torii 2011). The SiPM array consists of 64 individual Sensl type-60035 SiPM chips. There are two critical parameters for SiPMs, the break-down voltage  $V_{\rm bd}$  and over-voltage  $V_{\rm ov}$ .  $V_{\rm bd}$  of a SiPM is the minimum (reverse) bias voltage that results in selfsustaining avalanche multiplication.  $V_{ov}$  is equal to the SiPM bias voltage  $V_{\text{bias}}$  minus  $V_{\text{bd}}$ . The gain of a SiPM is proportional to the  $V_{\rm ov}$ . The  $V_{\rm bd}$  and  $V_{\rm ov}$  of the SiPM are typically 24.5 and 3.5 V at room temperature, respectively. As  $V_{\rm bd}$  is temperature dependent (the coefficient is typically 18 mV/°C derived from ground calibration) (Ramilli 2009), a thermal-compensation circuit is applied for GECAM to automatically adjust the SiPM operation voltage for stabilizing the SiPM gain according to the measured SiPM temperature (Zhang et al. 2019, 2022).

The output signal of the SiPM array is amplified at the first stage pre-amplifier and then fanned out in the second stage to two channels, e.g., the high-gain channel (HG) and the low gain channel (LG). The dynamic range of the high-gain and the low-gain channel is typically 8 keV–250 keV and 50 keV–5 MeV, respectively. The output pulse has a rise time around 200 ns and a fall time around 2  $\mu$ s. The pulse shape sampling is performed by a 40 MHz analog to digital converter (ADC), and the digital signals are analyzed in the Field Programmable Gate Array (FPGA) on the data acquisition (DAQ) boards. The algorithm implemented in FPGA can dynamically calculate the noise pedestal, identify the real events, and eventually record their peak amplitude with the pedestal subtracted (Liu et al. 2022). Meanwhile, the mean pedestal value of each channel will be saved in the housekeeping data once per second.

Before being transmitted to the satellite platform, the DAQ data are further processed in the payload data management (PDM) board. The PDM board organizes the event data (For each event, there are six bytes to record the arrival time and signal amplitude, etc.) and housekeeping data into 884 bytes data packet, respectively. Besides, the PDM boards also implement an onboard trigger and localization algorithm (Zhao et al. 2021) for real-time searching and locating potential GRBs according to the count rates of all the detectors.

## 3. In-flight Performance and Data Preparation

On 2020 December 10, twin satellites of GECAM were successfully launched from XiChang Satellite Launch Center in China. Unfortunately, both satellites encountered power supply issues. The detectors in GECAM-A cannot be powered on regularly yet, while the detectors in GECAM-B can operate for about 10 hr per day. Thus this paper only presents the in-flight calibration of GRDs onboard GECAM-B. Besides, most detectors are powered off when the satellites pass through the South Atlantic Anomaly (SAA) for safety.

We use the Level 1 hourly time-tagged events (TTE) data products for the in-flight energy calibration. Most of the hourly data are in-flight background including gamma-ray events originating from cosmic X-ray background (CXB), intrinsic radioactivity of the GRDs, albedo gamma-rays from atmosphere, radiation from the activated satellite materials (Guo et al. 2020) and also other particles, e.g., cosmic-rays and trapped charged particles in orbit. The hourly data are stored in Flexible Image Transport System (FITS) format. An automatic calibration pipeline has been developed to process the hourly data and generate raw calibration results. The pipeline starts with the following steps:

- The spectra of both high-gain channel and low-gain channel of all 25 detectors are accumulated using the hourly science data products. Prominent spectral lines are identified in the spectra and fitted with Gaussian distributions plus a continuous background.
- The mean and standard deviations of the SiPM temperature and bias voltages are calculated using the hourly housekeeping data products.
- 3. The pedestal spectra of all detector channels are accumulated using the amplitude of pedestal in the hourly housekeeping data products. Each spectrum is fitted with a Gaussian distribution to evaluate the mean and the sigma value of pedestal.

The typical high gain and low gain spectra of GRD accumulated in one hour are shown in Figure 1. The prominent peaks in high-gain are 37.4 and 85.8 keV, while the prominent peaks in low-gain are 511 and 1470 keV. The structure around 3500 ADC in low-gain is mainly contributed to the saturation of the amplifier circuit.

The 37.4 and 1470 keV peaks are generated by the internal <sup>138</sup>La decays via electron capture into <sup>138</sup>Ba in the LaBr3:Ce crystal (Deslattes et al. 2003; Torii 2011; Camp et al. 2016). These two peaks have already been reported in the ground test with GECAM GRDs (Zhang et al. 2019, 2022). On the other hand, the 85.8 keV and 511 keV peaks are absent in the ground test spectra (Deslattes et al. 2003; Torii 2011; Quarati et al. 2012; Camp et al. 2016; Zhang et al. 2019, 2022) but are clearly observed in the in-flight data. According to the GEANT4 simulation, both cosmic-rays and SAA protons can activate the satellite materials, while the latter makes the major contribution. When the 80Br nucleus of LaBr3 is activated into its excited state 80mBr, the cascaded de-excitation of the 80mBr emits a 48.8 and a 37.0 keV photon, resulting in the 85.8 keV peak jointly. Meanwhile, the 511 keV peak originates from the  $\beta$  decay in the activated materials (Nakazawa et al. 2018).

In this paper, we focus on the commission phase from 2020 December to 2021 June. The time evolution of the amplitude of the four prominent peaks is shown in Figure 2, and four stages

<sup>6</sup> http://fits.gsfc.nasa.gov

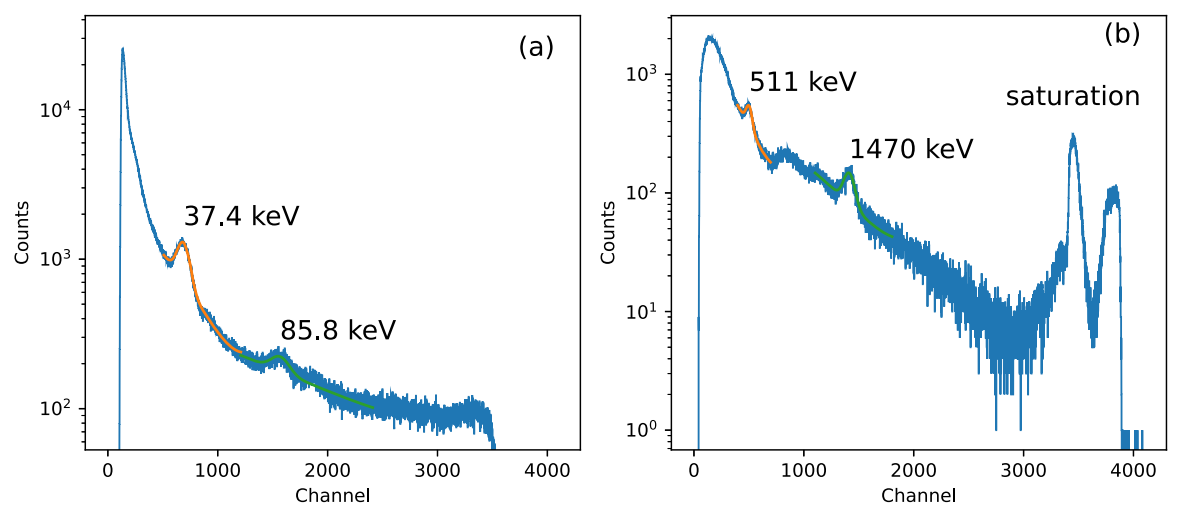


Figure 1. The in-flight spectra of the high-gain (a) and the low-gain (b) channels.

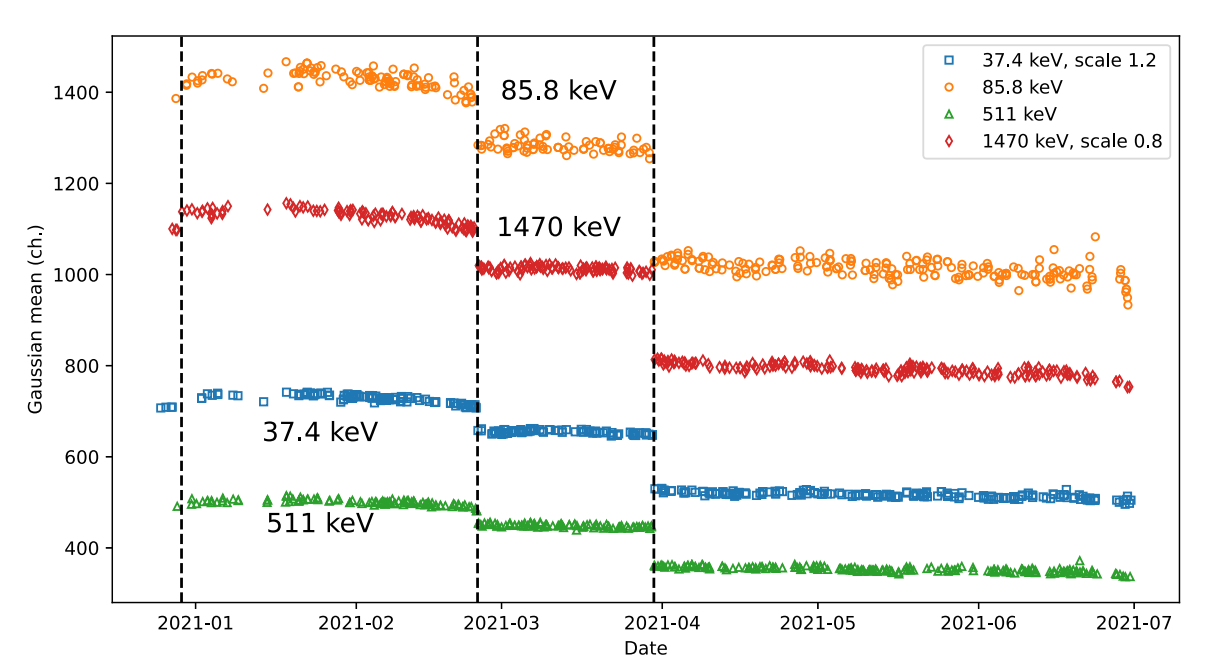


Figure 2. Evolution of the peak position for four characteristic lines. Data have been under-sampled for clear vision.

can be easily noticed. The three intersections between the four stages are December 29 in 2020, February 24 and March 30 in 2021, when the  $V_{\rm ov}$  of SiPMs was modified to suppress the dark count rates. However, the temperature coefficient k of  $V_{\rm bd}$  remains unchanged throughout all four stages.

In Figure 3, the time evolution of Gaussian sigma values of 37.4 and 1470 keV peaks is shown. For 37.4 keV, the evolution of the Gaussian sigma value is different from the peak position shown in Figure 2. The peak position is almost stable, but a quick increase in sigma values can be seen from 2020 December 29 to 2021 February 24. Meanwhile, the SiPM

current also has a synchronous increase. Their coincidence may be attributed to the accumulated radiation damage of the SiPMs (Qiang et al. 2013; Zhang et al. 2019) and the elevated temperature. On the contrary, the Gaussian sigma values of 1470 keV are stable within each stage, because this line is in the low gain channel and the dominant noise in the low gain channel comes from electronics rather than SiPM.

The 85.8 and 511 keV lines originate from short half-live radionuclides created by SAA proton activation. When the GRDs are powered on in the non-SAA region, the activities of 85.8 and 511 keV are mainly contributed by the delayed

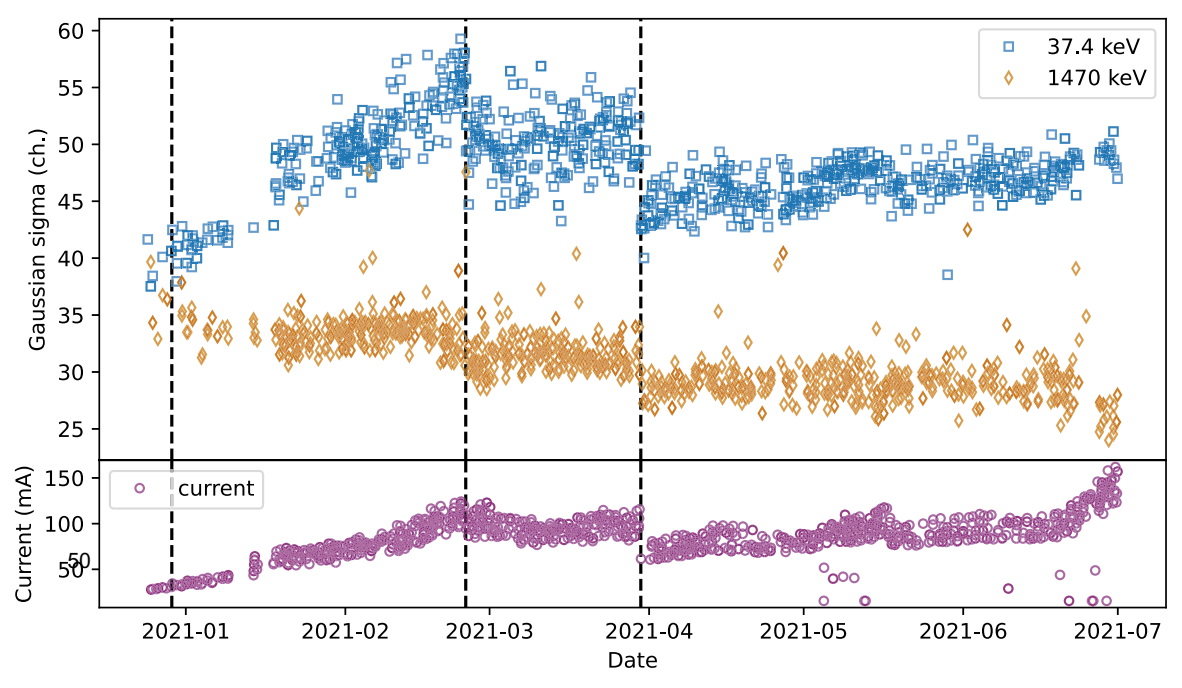


Figure 3. The evolution of the Gaussian sigma values of the characteristic lines and the SiPM current. Data have been under-sampled for clear vision.

radiation after passing SAA. As shown in Figure 1, they are relative weak compared to the continuum background, especially when the GECAM-B satellite does not pass SAA for a period of time, say several hours. As a result, the 85.8 and 511 keV peaks with low statistics are not used in the energy resolution calibration.

## 4. Energy-channel Relation Calibration

The conversion from Level-0 data (in raw ADC channel) to Level-1 data (in PI channel, keV) relies on the energy-channel (i.e., E-C) relations stored in the calibration database (CALDB). So, this section focuses on the procedure in calibrating the energy-channel relation.

Many previous studies have found that the LaBr3:Ce scintillators have non-proportionality response (nPR) in the light yield (Quarati et al. 2013; Musienko et al. 2020). The nPR of all the GRDs have been measured on the ground using the Hard X-ray Calibration Facility (HXCF) and radioactive sources at China National Institute of Metrology. The energies of mono-energetic X-rays generated by HXCF range from 8 to 160 keV, while the energies of the radiation sources range from 390 keV to 1.8 MeV. The exact X-ray energy of HXCF in each measurement was calibrated with a standard high-purity germanium (HPGe) detector. Besides, we also accumulated the background spectra of GRDs before or after each measurement of mono-energetic X-rays. Therefore, the gain drift of SiPMs in different measurements could be easily

eliminated with the help of characteristic lines i.e., 37.4 and  $1470\,\mathrm{keV}$ .

As an example, the ground calibrated energy-channel relation and the nPR of the GRD01 is shown in Figure 4. The nPR value is normalized to 100% at 661.66 keV. It is clear that the nPR curve has two breaks at the characteristic energy corresponding to the K-shell binding energy of Br (13.47 keV) and La (38.93 keV). The breaks in the light outputs just above the K-shell binding energy are attributed to the low light-yield of the K-shell photoelectrons deposited in LaBr3:Ce scintillator (Zheng et al. 2022).

Consequently, the energy-channel relation of GRD could be parameterized with several segmented polynomial functions to describe the nPR with breaks. As shown in Figure 5(a), the dynamic range of high-gain channel fully covers the two K-shell binding energy (13.47 and 38.93 keV). So, three segmented quadratic functions were used to fit the E-C relation in the energy below the Br K-edge, between the Br and La K-edges, and above the La K-edge respectively. However, the fit functions around the K-edge energy have discrepancies which was also reported by Fermi GBM (Owens et al. 2007b). These discrepancies lead to ambiguity in the conversion from channel to energy. An optional solution is to take the mean value derived from the two energy-channel relations (Owens et al. 2007b), i.e., using linear function to connect the discontinuity around the K-edge. For the low-gain channel, the E-C relation can be easily parameterized with a single

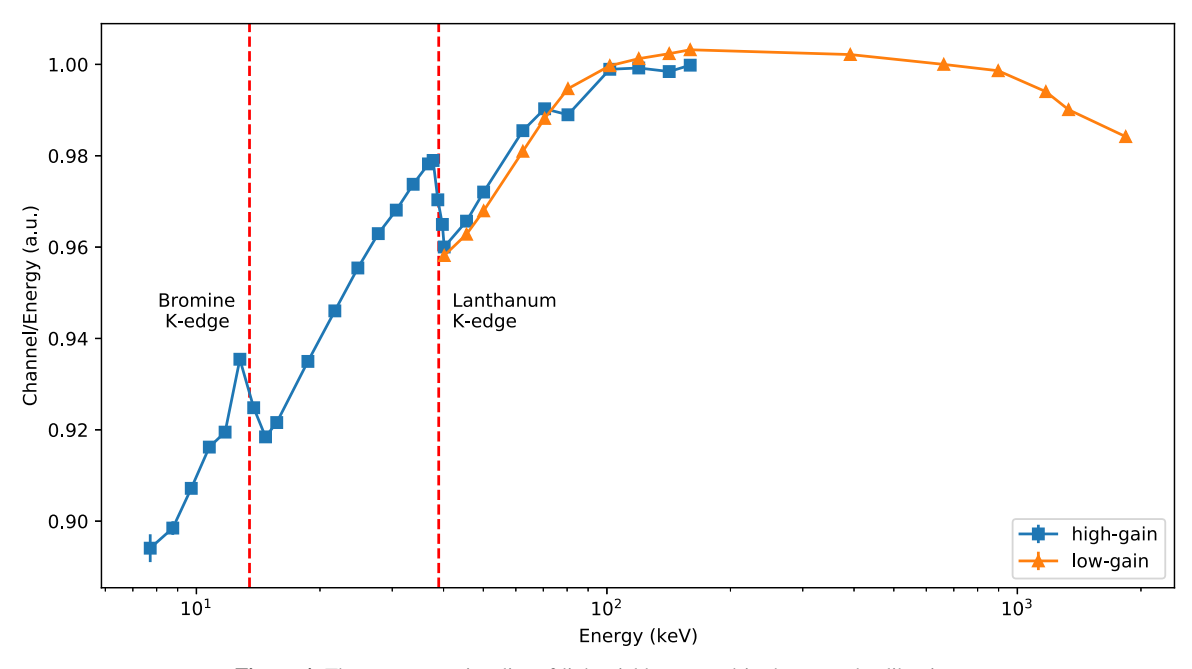


Figure 4. The non-proportionality of light yield measured in the ground calibration.

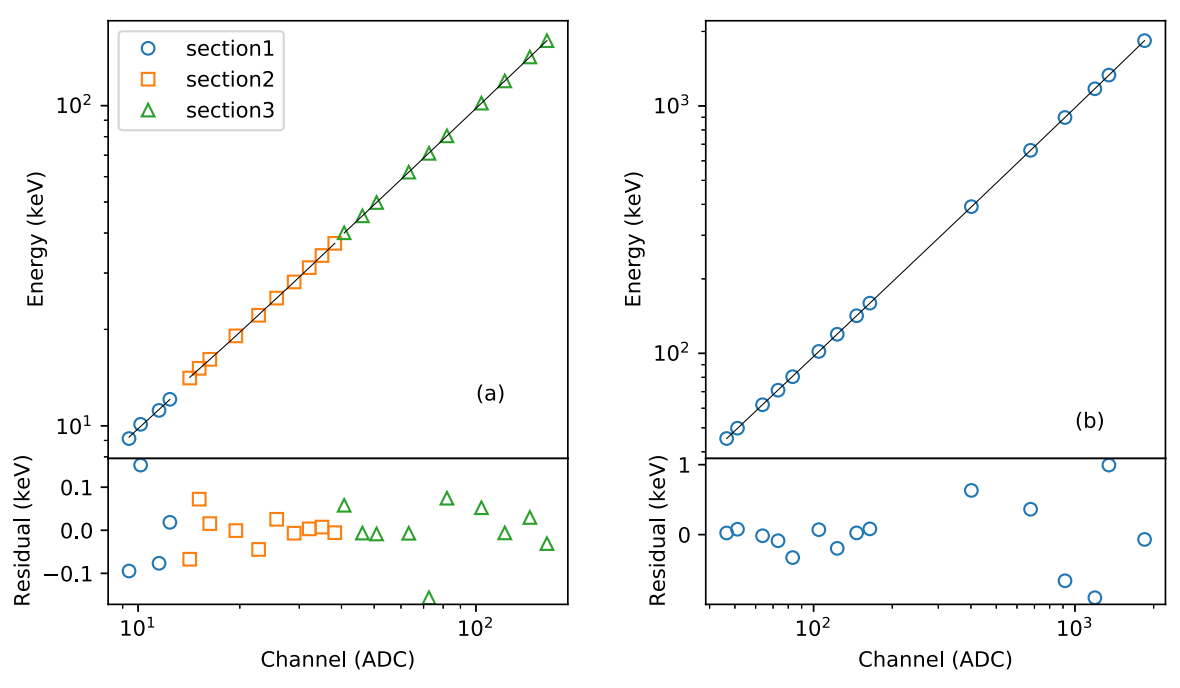


Figure 5. The energy-channel relation of the GRD high-gain channel (a) and low-gain channel (b).

quadratic function, because no K-edge exists in the low-gain channel above  $50\,\mathrm{keV}$ .

In fact, the in-flight gain of GRD is continuously changed with the modified over-voltage and the degradation of SiPM, as shown in Figure 2. However, we can use two intrinsic lines

(37.4 and 1470 keV) and activated 511 keV line in the background spectra to track the gain variation in orbit.

In order to compare with the ground calibration results, we plot the in-flight peak positions of 37.4, 511 and 1470 keV at four different times in Figure 6. Because the high-gain channel

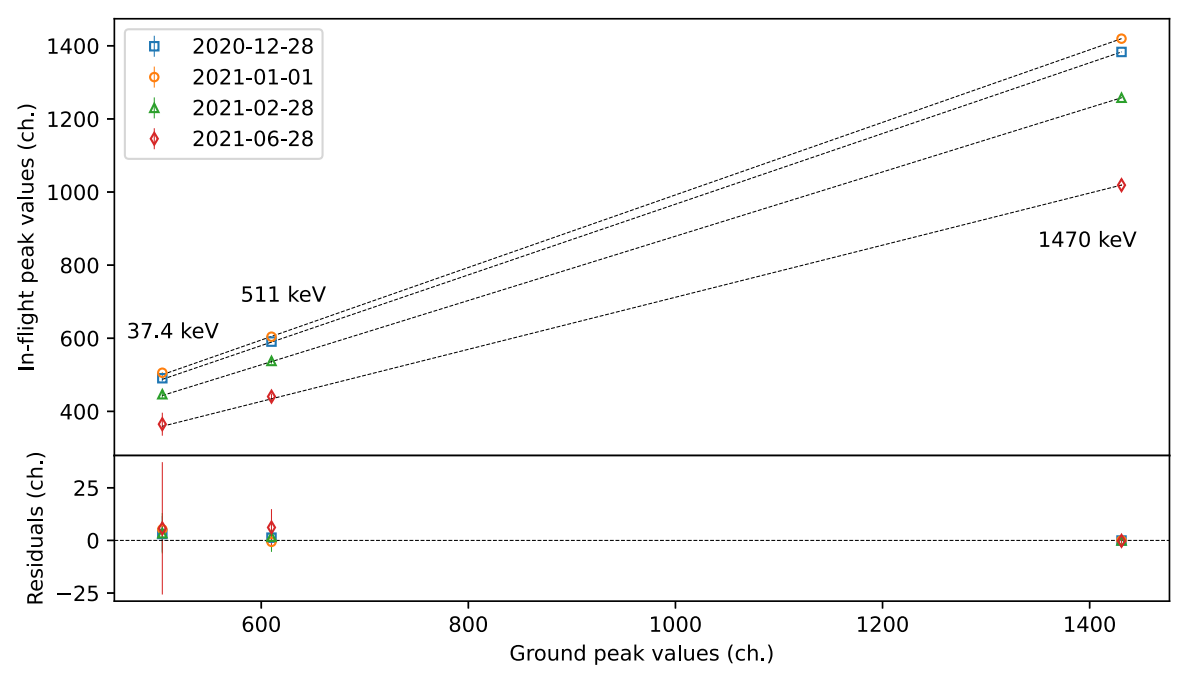


Figure 6. Correlation of amplitude of the three known lines between the ground and in-flight measurements.

and the low-gain channel of a GRD share the same LaBr3:Ce crystal and SiPM array in each GRD, the gain of high-gain and low-gain channels will change simultaneously and the relative change could be evaluated by the slope of linear fitting implemented in Figure 6. During the linear fitting, the intercept is fixed to zero, because the pedestal has been automatically subtracted in the DAQ algorithm.

$$\begin{cases} P_{2,\text{flight}} = \frac{P_{2,\text{gnd}}}{m^2} \\ P_{1,\text{flight}} = \frac{P_{1,\text{gnd}}}{m} \\ P_{0,\text{flight}} = P_{0,\text{gnd}} \end{cases}$$

$$(1)$$

From the fitting results, we can learn that the gain variation is approximately  $\pm 1\%$  within each stage, while the gain change significantly between adjacent stages (e.g., 20% decrease from stage 3 to stage 4). As a result, individual calibration product of the energy-channel relation should be generated for each stage. Each calibration product consists of 50 FITS format files for high-gain and low gain channels of 25 GRDs. Each FITS file stores the quadratic parameters of the nPR for high-gain or low-gain channel. Based on the ground calibrated nPR, the in-flight nPR parameters can be calculated by formula (1), where  $P_2$ ,  $P_1$  and  $P_0$  are the parameters of the quadratic function of the GRD nPR, and m is the mean value of the relative change of gain during each stage.

## 5. Energy Resolution Calibration

The Energy Resolution Function (ERF) of GRD is required in the production of GRD energy response matrix. In the ground test, we have modeled the energy resolution of GRDs using quadratic functions, as shown in Figure 7:

$$\begin{cases} \sigma_h^2 = P_2 E^2 P_1 E P_{0,h} \\ \sigma_l^2 = P_2 E^2 P_1 E P_{0,l} \end{cases}$$
 (2)

Here  $\sigma_h$  and  $\sigma_l$  are the energy resolution of the GRD highgain and low-gain channels, respectively. The first term with  $P_2$ is attributed to the nPR of scintillators. The second term with  $P_1$  is the contribution from the statistical fluctuation which is proportional to the incident gamma-ray energy.  $P_0$  is the constant contribution independent of the gamma-ray energy, which is the sum of squares of the SiPM dark noise and the electronic noises (Bissaldi et al. 2009; Moszynski et al. 2016). As mentioned above, the high-gain and low-gain channels share the same scintillator and SiPM in one GRD, therefore the two channels have the same parameter values for  $P_1$  and  $P_2$ .  $P_{0,l}$  is always larger than  $P_{0,h}$  because the low-gain channel has higher electronic noise than the high-gain channel. Although the quadratic function in formula (2) has been parameterized via ground calibration, they should be re-calibrated in flight due to the change of in-flight detector status, such as the progressive increase of SiPM dark current. However, only two remarkable peaks (i.e., 37.4 and 1470 keV) can be used for in-flight energy resolution calibration as described in Section 3.

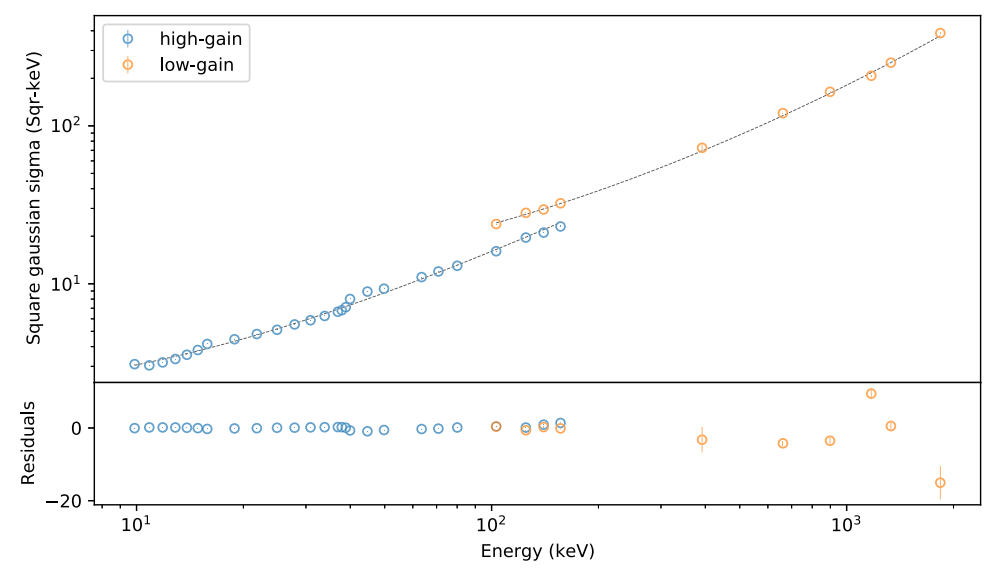


Figure 7. Ground calibration of the energy resolution.

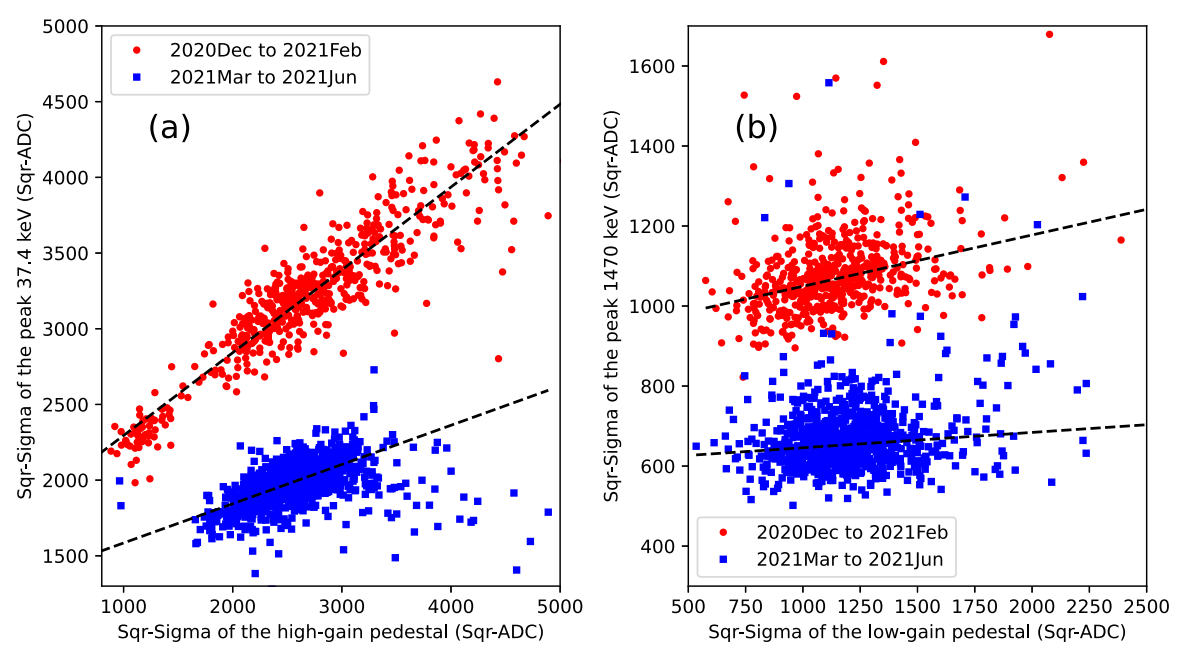


Figure 8. Square sigma correlation between the intrinsic activities and pedestal: (a) the peak 37.4 keV verses the high-gain pedestal, (b) the peak 1470 keV verses the low-gain pedestal.

Fortunately, for each channel, the pedestal data can be used to describe the SiPM dark noises and the electronic noises, i.e., the constant term  $P_0$  in formula (2). Thereby, we can replace  $P_0$  with the in-flight noise level of pedestal:

$$\begin{cases}
\sigma_h^2 = P_2 E^2 P_1 E \kappa_h \sigma_{\text{pds},h}^2 \\
\sigma_l^2 = P_2 E^2 P_1 E \kappa_l \sigma_{\text{pds},l}^2
\end{cases}$$
(3)

Here  $\sigma_{\mathrm{pds},h}$  and  $\sigma_{\mathrm{pds},l}$  are the sigma values of the Gaussian distribution of pedestal in the high-gain and low-gain channels, respectively.  $\kappa$  is the coefficient originating from the different DAQ modes (Liu et al. 2022). As demonstrated in Figure 8, there is a linear relationship between  $\sigma_h^2$  and  $\sigma_{\mathrm{pds},h}^2$  as well as between  $\sigma_l^2$  and  $\sigma_{\mathrm{pds},l}^2$ . As a result, the square sigma correlation in Figure 8 can be fitted with linear functions, where the ratios

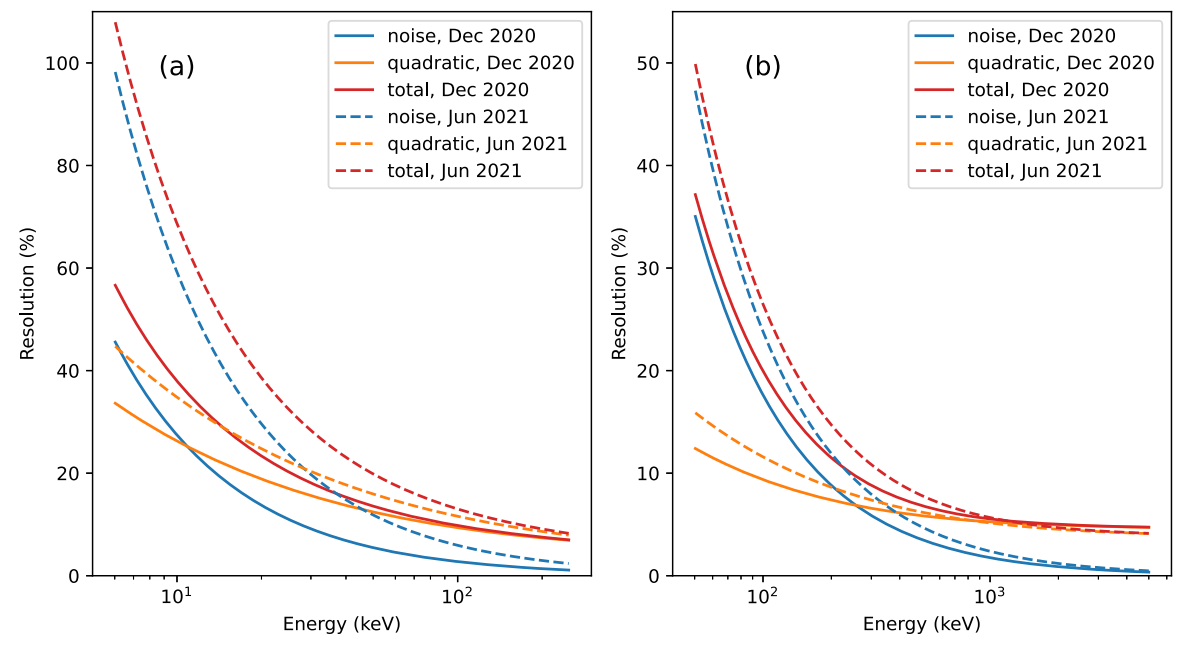


Figure 9. In-flight energy resolutions of GRD high-gain (a) and low-gain (b) channels.

 $\kappa$  are evaluated by the fit slopes, meanwhile  $P_2$  and  $P_1$  can be derived with the fit intercept. As long as the parameters of the thermal-compensation circuit are fixed,  $P_2$  and  $P_1$  in formula (3) will remain constant.

In addition, special attention should be paid to the 1470 keV peak which is actually composed of several peaks. The major peak is a combination of 1436 keV  $\gamma$ -ray from the <sup>138</sup>Ba deexcitation and 32 keV K  $\alpha$  line of Ba. Several minor peaks are the combination of 1436 keV and other characteristic X-rays of Ba with energies ranging from 31 to 38 keV (Quarati et al. 2012). Consequently, we should subtract the contribution of minor peaks from  $\sigma_l^2$  in drawing Figure 8.

The in-flight calibrated energy resolution, normally defined as the FWHM of the Gaussian divided by the energy (i.e.,  $2.35\sigma/E$ ), is shown in Figure 9. The solid curves are taken from the results when the satellite was operated for the first month after launch. For the high-gain channel, the resolution of energy above 10 keV is mainly contributed by the quadratic components which are originated from the scintillator nPR and statistic fluctuation. On the other hand, the noise (mainly the electronic noise) dominates in the GRD low-gain channel up to 200 keV. The cumulative radiation damages in space cause the increase of the SiPM dark noise. The energy resolutions became worse after six months of in-flight operation, as shown in Figure 9 in dashed curves. Due to the radiation damage of SiPMs, the energy resolution gradually increased (from approximately 12% to 18% at 59.6 keV). In order to slow down the increase of the SiPM dark current, the  $V_{ov}$  of SiPMs

was reduced, which consequently worsened the energy resolution.

For each stage, the calibration products of energy resolution have been generated. Each calibration product consists of in total 50 FITS files, corresponding to the high-gain and low-gain channels of 25 GRDs. Each FITS file stores a matrix describing the energy spread response due to the energy resolution.

# 6. Energy Response Matrix and Spectral Crosscalibration

Detector response matrices (DRMs) are essential for the spectral analysis. We construct a calibration database (CALDB) and develop a corresponding DRM generator tool for GECAM. In the CALDB, we store the in-flight calibration products, as well as the deposited energy response matrices (DERMs) simulated for each GRD. The simulations were implemented in Geant4 with a precise mass model of GECAM satellite and run for 500 incident directions covering the all-sky with input gamma-ray energies range from 2 keV to 40 MeV.

For a celestial source detected by GRDs, the DRM generator will first perform a spatial interpolation to achieve the DERMs of the incident direction. Then the DERMs are convolved with in-flight energy resolution matrices to yield DRMs.

In order to assess the accuracy of GRD DRMs, several detected GRBs (GRB 210 121A, GRB 210 511B, etc.) are used to cross-calibrate GECAM GRDs with the Fermi/GBM (Wang et al. 2021; Xiao et al. 2022). Here, we just give one example: GRB 210 514A is simultaneously observed by both GECAM-B and Fermi/GBM. We perform a joint fit in the Xspec with the

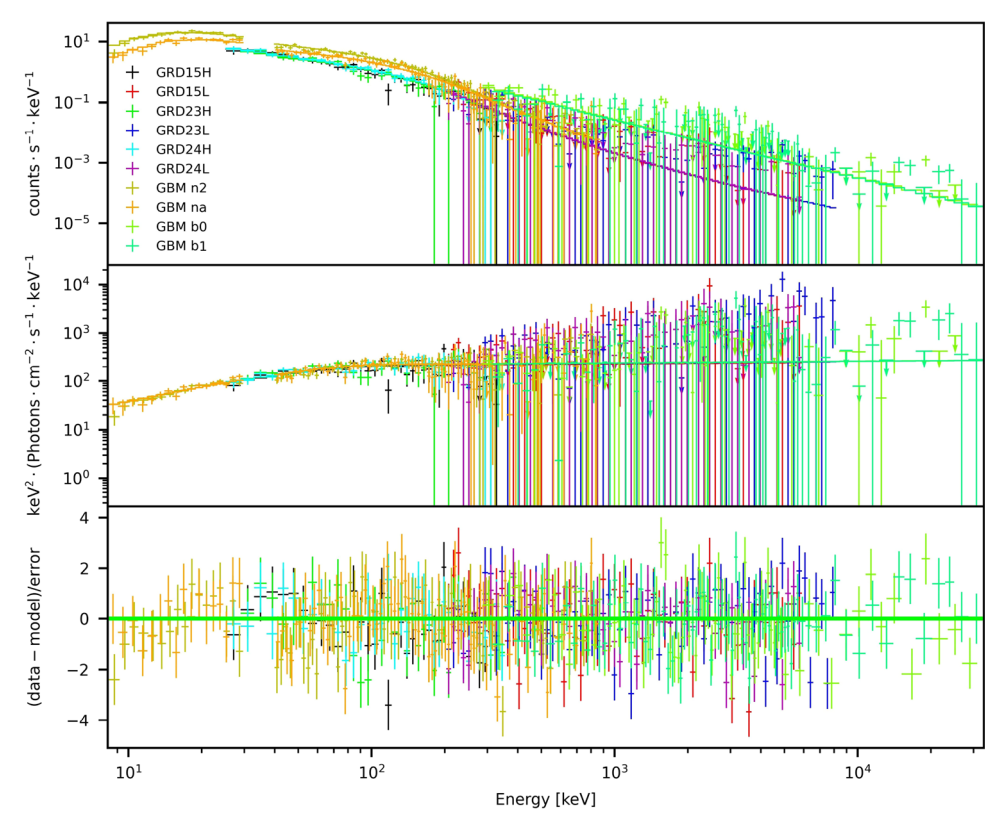


Figure 10. Joint spectral fit results with GRD and Fermi GBM using GRB 210 514A.

Band model (Band et al. 1993), as shown in Figure 10. The residuals for the spectra are mostly constrained within  $\pm 2\sigma$ . The goodness of the fits is evaluated using the pgstat (Poisson data with Gaussian background) with pgstat/dof = 790/664 = 1.19. A systematic study of cross-calibration will be present in a separate work.

#### 7. Conclusion

GECAM equipped with LaBr3:CeSiPM detectors is a dedicated mission for GRB detection. In this work, we present the methodology and results of in-flight energy calibration, in which four prominent peaks (37.4, 85.8, 511, and 1470 keV) of the in-flight background spectra are used. Obviously, the performance degradation of GRDs are highly related to the cumulative radiation damages of SiPMs. Hence, the overvoltage of SiPM has been tuned down to reduce the growth rate of the SiPM dark current. Indeed, there is a compromise between the gain and noise of SiPM. After six months of operation, the over-voltages decreased by 1 volt, resulting in a 30% decrease in the SiPM gain. Meanwhile the energy resolution contributed by the dark noise has been increased from 12% to 18% at 59.6 keV.

The in-flight energy calibration products, including E-C relations and energy resolution functions, have been produced

four times during the commission phase, corresponding to the four stages with different SiPM over-voltages. The calibration products are used to automatically generate Level-1 data and energy response matrix for the observed astronomical bursts. Besides, the spectral cross-calibrations of GECAM GRDs and Fermi/GBM show that they are in good agreements, which demonstrate that the energy response matrix of GRDs are ready for the data analysis.

# Acknowledgments

This research is supported by the Strategic Priority Program on Space Science, the Chinese Academy of Sciences, grant Nos. XDA15360102, XDA15360300 and E02212A02S, and the National Natural Science Foundation of China (Project: 12061131007).

### **ORCID** iDs

Rui Qiao ® https://orcid.org/0000-0001-7398-0298 Li-Ming Song ® https://orcid.org/0000-0003-0274-3396 Yue Huang ® https://orcid.org/0000-0002-3515-9500

#### References

Abbott, B. P., Abbott, R., Abbott, T. D., et al. 2017, ApJL, 848, L13 An, Z. H., Sun, X. L., Zhang, D. L., et al. 2022, RDTM, 6, 43 Band, D., Matteson, J., Ford, L., et al. 1993, ApJ, 413, 281

```
Bissaldi, E., von Kienlin, A., Lichti, G., et al. 2009, ExA, 24, 47
Camp, A., Vargas, A., & Fernandez-Varea, J. M. 2016, AppRI, 109, 512
Deslattes, R., Kessler, E., Indelicato, P., et al. 2003, RvMP, 75, 35
Drozdowski, W., Dorenbos, P., Bos, A. J. J., et al. 2007, ITNS, 54, 736
Guo, D., Peng, W., Zhu, Y., et al. 2020, SSPMA, 50, 129509
Iltis, A., Mayhugh, M. R., Menge, P., et al. 2006, NIMPA, 563, 359
Li, X. Q., Wen, X. Y., An, Z. H., et al. 2022, RDTM, 6, 12
Liu, Y. Q., Gong, K., Li, X. Q., et al. 2022, RDTM, 6, 70
Meegan, C., Lichti, G., Bhat, P. N., et al. 2009, ApJ, 702, 791
Moses, W. 2002, NIMPA, 487, 123
Moszynski, M., Nassalski, A., Syntfeld-Kazuch, A., et al. 2006, NIMPA,
  568, 739
Moszynski, M., Syntfeld-Kazuch, A., Swiderski, L., et al. 2016, NIMPA,
   805, 25
Musienko, Y., Heering, A., Karneyeu, A., & Wayne, M. 2020, JInst, 15,
   C09036
Nakazawa, K., Sato, G., Kokubun, M., et al. 2018, JATIS, 4, 021410
Normand, S., Iltis, A., Bernard, F., Domenech, T., & Delacour, P. 2007,
   NIMPA, 572, 754
```

```
Owens, A., Bos, A. J. J., Brandenburg, S., et al. 2007a, NIMPA, 572,
Owens, A., Bos, A. J. J., Brandenburg, S., et al. 2007b, NIMPA, 574, 158
Qiang, Y., Zorn, C., Barbosa, F., & Smith, E. 2013, NIMPA, 698, 234
Quarati, F. G. A., Dorenbos, P., van der Biezen, J., et al. 2013, NIMPA,
  729, 596
Quarati, F. G. A., Khodyuk, I. V., van Eijk, C. W. E., Quarati, P., &
  Dorenbos, P. 2012, NIMPA, 683, 46
Ramilli, M. 2008, in IEEE Nuclear Science Symp. Conf. Record (Piscataway,
  NJ: IEEE), 2467
Savchenko, V., Ferrigno, C., Kuulkers, E., et al. 2017, ApJL, 848, L15
Torii, S. 2011, NIMPA, 630, 55
Von Kienlin, A., Meegan, C., & Goldstein, A. 2017, GCN, 21520, 1
Wang, X. I., Zheng, X., Xiao, S., et al. 2021, ApJ, 922, 237
Xiao, S., Xiong, S.-L., Cai, C., et al. 2022, MNRAS, 514, 2397
Zhang, D., Li, X., Wen, X., et al. 2022, NIMPA, 1027, 166222
Zhang, D., Li, X., Xiong, S., et al. 2019, NIMPA, 921, 8
Zhao, X.-Y., Xiong, S.-L., Wen, X.-Y., et al. 2021, arXiv:2112.05101
Zheng, C., Peng, W. X., Li, X. B., et al. 2022, NIMPA, 1042, 167427
```